Supporting Information for: "Projections of 21st Century Sea-Level Fall Along Coastal Greenland"

Lauren Lewright*[1], Jacqueline Austermann[1], Christopher G. Piecuch[2], Surendra Adhikari[3], James L. Davis[1], Glenn A. Milne[4], and Guy J. G. Paxman[5]

[1]Lamont-Doherty Earth Observatory, Columbia University

[2]Physical Oceanography Department, Woods Hole Oceanographic Institution

[3]Jet Propulsion Laboratory, California Institute of Technology

[4]University of Ottawa

[5]Department of Geography, Durham University

*llewright@ldeo.columbia.edu

Contents of this file:

Supplementary Section 1: Calculation of the reference-frame contribution to observed present-day VLM

There may be differences in the reference frame used in the GIA model versus that of the VLM observations and these need to be accounted for when comparing predictions from the former to the latter. In our GIA model, the reference frame is the center of mass of the solid Earth. The exact reference frame of the GNSS observations is unknown. The reference frame correction assumes that any shift between the model predictions and observations that is consistent with a difference in reference frame is indeed driven by a difference in reference frame, and is therefore removed (Lidberg et al., 2007; Hill et al., 2010). We account for the difference between the center of mass of the solid Earth reference frame and the unknown GNSS reference frame by considering that this difference can be described as:

$$V_{OBS} - V_{deglacial} - V_{LIA} - V_{ELA} = T_x \cos\phi \cos\lambda + T_y \cos\phi \sin\lambda + T_z \sin\phi \qquad \text{(Supplementary Eq. 1)}$$

where $\boldsymbol{T} = (T_x, T_y, T_z)$, a parameter in the Helmert transformation, is the unknown reference frame translation rate in a Cartesian coordinate system and ϕ and λ are latitude and longitude, respectively, of each station location. We estimate $\boldsymbol{T}$ using a least squares approach that minimizes the distance between the reference frame correction (right side of Supplementary eq. 1) and the residual observed VLM (left side of Supplementary eq. 1) for each of the 14,040 predictions of V_{LIA}.

Supplementary Section 2: Time series of relative sea level (RSL) to 2100 CE for RCP 2.6 and RCP 8.5 for 6 towns/settlements located around Greenland's coast

Time series of RSL from 2017 CE to 2100 CE for RCP 2.6 and RCP 8.5 (Supplementary Fig. 5) show that sea level will fall throughout this century for six selected settlements located around

Greenland's coast. These locations were chosen based on the size of their population and/or their proximity to large marine-terminating glacier systems. Tasiilaq and Ilulissat are projected to experience the largest RSL fall out of the six settlements as they are both located near large marine-terminating glaciers (Helheim Glacier and Sermeq Kujalleq, respectively) that are projected to lose significant amounts of mass. Tasiilaq is projected to experience a RSL fall by 2100 CE amounting to -0.58 m [-0.83 m to -0.38 m] and -1.4 m [-1.8 m to -0.95 m] for RCPs 2.6 and 8.5, respectively. The likely range at this location is large because of its proximity to Helheim Glacier, the behavior of which over the next century is highly uncertain (Figure 4f, 4h). Ilulissat has a population of 4,413 and is projected to experience a RSL fall by 2100 CE of -0.64 m [-0.87 m to -0.42 m] for RCP 2.6 and -1.4 m [-1.8 m to -1.1 m] for RCP 8.5. Similarly to Tasiilaq, the contribution to RSL associated with projected ice-sheet mass change dominates this signal.

Qaqortoq is located in southern Greenland and has a population of a little under 3,000 inhabitants. RSL here is projected to fall by -0.45 m [-0.64 m to -0.27 m] for RCP 2.6 and -0.98 m [-1.3 m to -0.70 m] for RCP 8.5 by 2100 CE. Nuuk, the capital of Greenland and the most populated area on the island with 19,611 inhabitants, is projected to experience a similar RSL fall by the end of the 21st century of -0.35 m [-0.55 m to -0.15 m] and -0.83 m [-1.2 m to -0.54 m] for RCPs 2.6 and 8.5, respectively. Both of these locations have a similar magnitude LIA contribution to RSL, but Nuuk experiences a greater RSL rise driven by deglacial ice loss and a smaller RSL fall from future ice loss than Qaqortoq. This means the total projected RSL fall is marginally lower in amplitude in Nuuk compared to Qaqortoq. The smaller RSL fall projected for these two locations compared to Tasiilaq and Ilulissat can be attributed to their greater distance from the modern ice margin, where contemporary and projected ice loss is focused.

Kullorsuaq, located on the northwestern coast of Greenland, has a population of about 500 people. Projections of RSL fall at 2100 CE for this area reach values of -0.53 m [-0.75 m to -0.31 m] for RCP 2.6 and -1.3 m [-1.6 m to -0.97 m] for RCP 8.5. RSL in Pituffik, which is located slightly north of Kullorsuaq and serves as a space base with nearly 600 inhabitants, is projected to fall by -0.49 m [-0.72 m to -0.27 m] and -1.2 m [-1.5 m to -0.87 m] by 2100 CE for RCP 2.6 and RCP 8.5, respectively. Because of Pituffik's proximity to the Canadian Arctic, RSL fall caused by Canada's peripheral glacier melt nearly balances out the RSL rise driven mainly by thermal expansion and ocean dynamics. The deglacial contribution to RSL in Pituffik is virtually 0 m, meaning that RSL change seen at this location over this century is mainly due to LIA and future ice-sheet loss.

Supplementary Section 3: Validation of the Bayesian model used in this study

We made a histogram of $\boldsymbol{x}$ to investigate the distributional shape of the LIA' VLM data (Supplementary Fig. 6). From this, we decided that it was justifiable to model the data using a Gaussian distribution. More generally, to assess whether the model's design is appropriate given the data, we evaluate residual differences $x - v$ (Equation 4) and $v - u$ (Equation 5). We see that residuals are centered on zero and appear randomly distributed, without any obvious spatial structure or systematic pattern, which is consistent with our assumption that residuals behave as zero-mean random i.i.d. white noise (Supplementary Figs. 7a, 7d). Further, scales and magnitudes of uncertainties on the residuals (Supplementary Figs. 7b, 7e) are qualitatively consistent with expectations given the data errors (Supplementary Fig. 7c) and solutions for other parameters (Supplementary Fig. 7f). Thus, the residual analysis shows that posterior solutions do not grossly violate our modeling assumptions, suggesting that the model is useful for present purposes. To evaluate convergence of the solutions, we ran multiple parallel simulations and computed the R-hat (Gelman-Rubin) statistic based on the ratio of between-chain and within-chain variance (Supplementary Fig. 8). R-hat values were ~1 for all parameters, meaning that solutions have converged. We also performed leave-one-out cross validation to quantify skill. We ran 55 separate model experiments, each which omitted data from one of the 55 GNSS stations. Then, we used the model equations to make a prediction at the location of the omitted data, which was then compared to the withheld data itself to evaluate model performance. We found that, on average, mean absolute errors between the withheld data and model predictions were ~1 mm/yr (Supplementary Fig. 9). Additionally, posterior coverage rates were determined to be accurate, for example, such that posterior 95% credible intervals capture roughly 95% of the true withheld values (Supplementary Fig. 9 inset).

We have demonstrated that our model is appropriate given the data, but it is an open question whether alternative model structures (e.g., choosing a different distributional shape in the data-level equation, such as a skew-normal, or the form of covariance function in the process-level equation, such as a Mátern) would substantially alter the results. A definitive determination would require a dedicated modeling investigation to quantify the influence of such modeling choices on posterior solutions, which we leave to a future study

Reference	# of models used	Ice History	Seismic Tomography model	Lithospheric Thickness model	Background Viscosity
Pan et al. (2022)	**40** from published paper and **20** adapted from the same Earth and ice models used in the paper	ICE6G ANU	S40RTS Savani SEMUCB-WM1 SL2013sv Combination of SL2013sv and S40RTS	Afonso et al. (2019) Yousefi et al. (2021)	UMV: 2x10^{20}, LMV: 3x10^{22} UMV: 3x10^{20}, LMV: 2x10^{21} VM2, Peltier (2004)
Austermann et al. (2021)	**4**	ICE6G	SL2013sv (< 400 km depth) & SEMUCSB-WM1 (> 400 km depth)	LT: 100 km, UMV: 5x10^{20}, LMV: 5x10^{21} LT: 80 km, UMV: 5x10^{20}, LMV: 5x10^{21} VM5 (Peltier & Drummond, 2008)	
Antwerpen et al. (2024)	**1**	HUY3	SL2013sv (< 400 km depth) & SEMUCSB-WM1 (> 400 km depth)	LT: 100 km, UMV: 5x10^{20}, LMV: 5x10^{21}	

Supplementary Table 1: Suite of 65 3D GIA model runs. Model output was used to create the weighted average of present-day vertical-land motion caused by the deglaciation. See Methods for details on how predictions from each GIA model run were weighted.

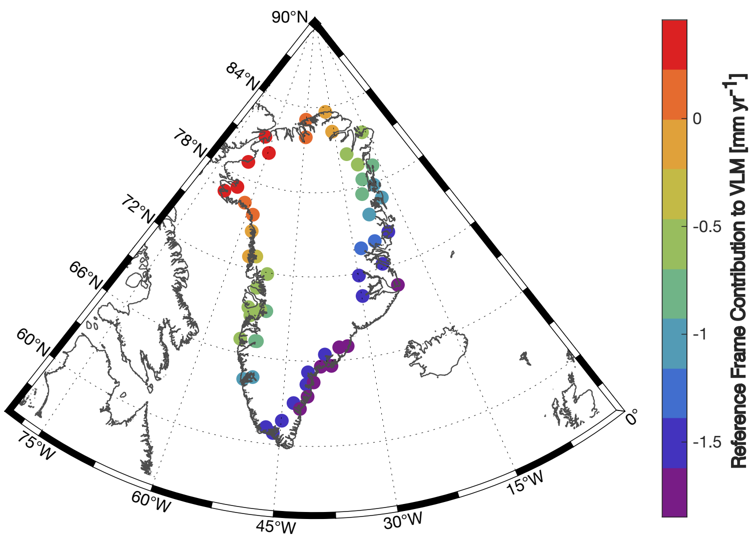

Supplementary Figure 1: **Reference-frame contribution to present-day vertical-land motion observations.** Circles represent the locations of Greenland's 55 Global Navigation Satellite System stations used in this study.

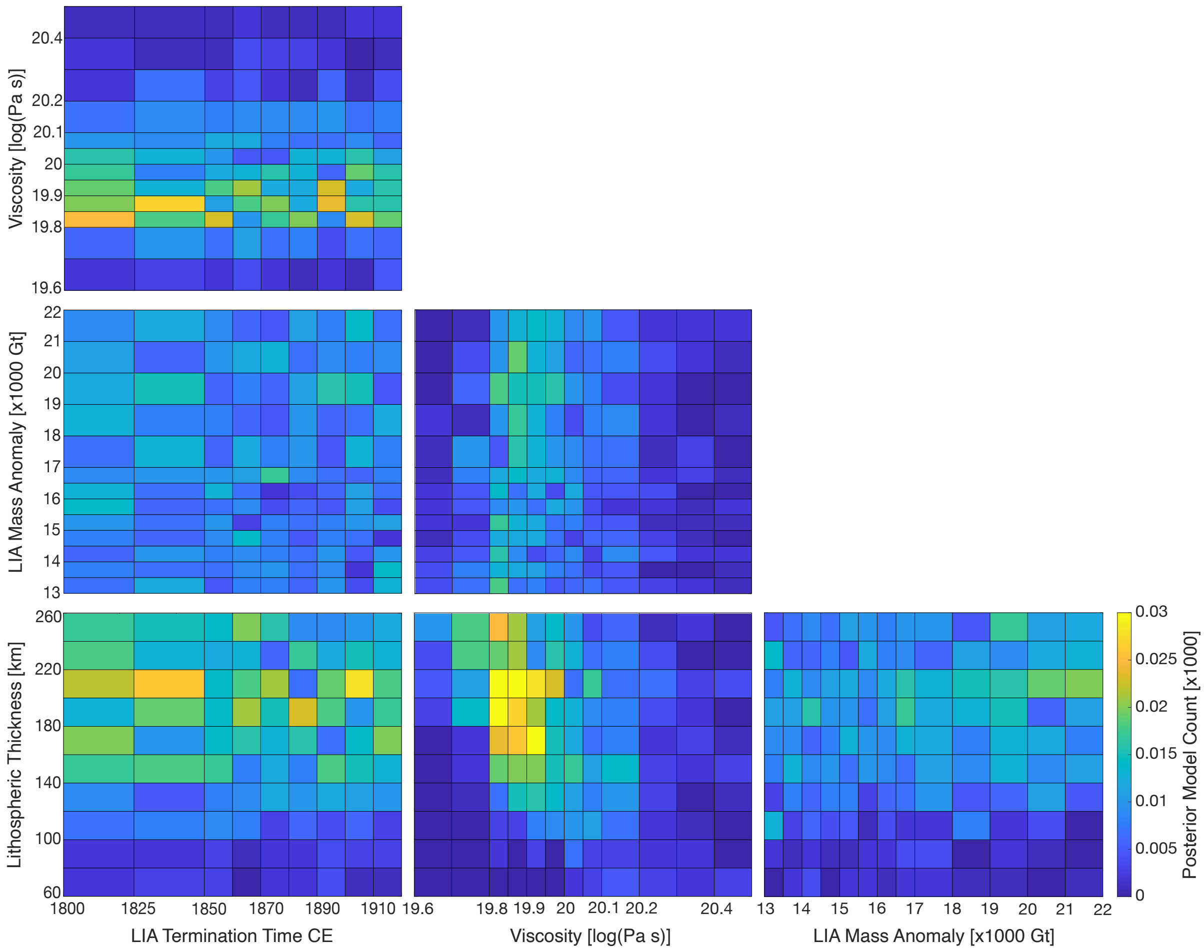

Supplementary Figure 2: **Posterior covariance between parameters varied in the 1D GIA model**. Parameters (Table 1 in main text) were used to create a suite of GIA model runs to calculate present-day vertical-land motion caused by the Little Ice Age (LIA) and projections of RSL change caused by ice changes from the LIA-2100 CE. The color of each grid cell represents the number of times a parameter combination was "picked" in our Bayesian inversion.

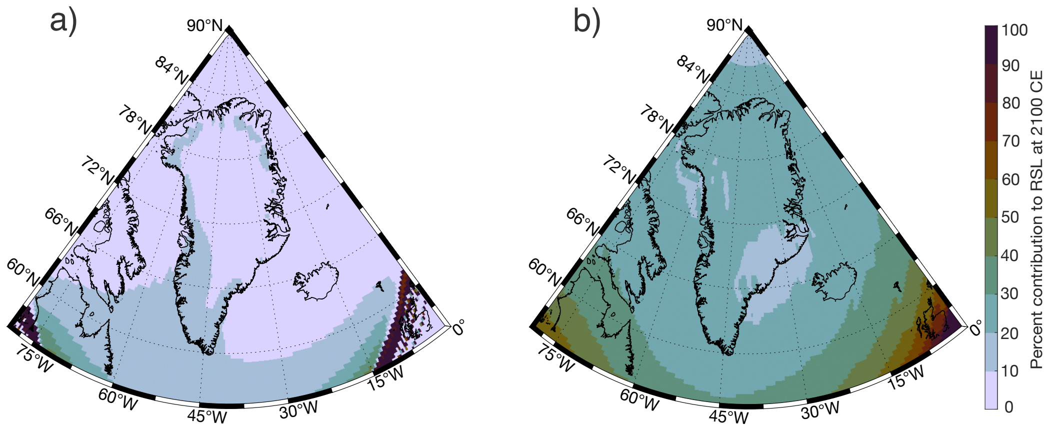

Supplementary Figure 3: **The contribution of gravitational effects to relative sea-level change at 2100 CE relative to 2017 CE.** The percent contribution of the gravitational response to relative sea-level change driven by Little Ice Age-to-2100 CE mass changes for RCP 2.6 a) and RCP 8.5 b). The percent contribution is calculated for each of the 8 ice-sheet projections considered in this study (Goelzer et al., 2020; Seroussi et al., 2020) and the mean is shown here.

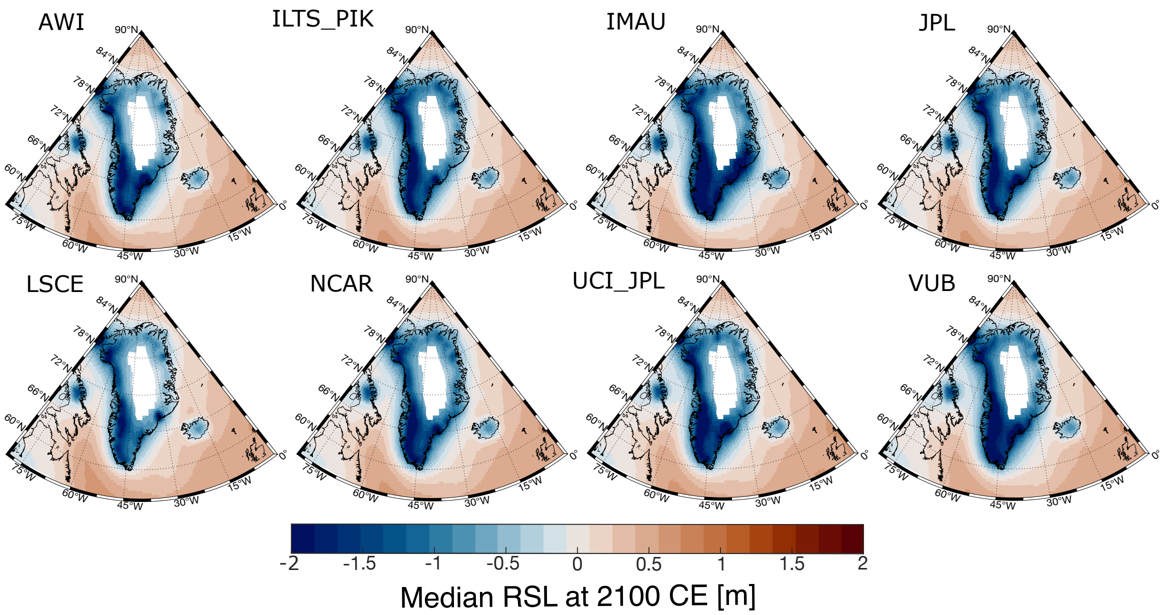

Supplementary Figure 4: **Projections of relative sea-level (RSL) change at 2100 CE relative to 2017 CE for different ice-sheet projections under RCP 8.5**. Ice-sheet projections are from the 8 individual ice-sheet modeling groups considered in this study: AWI, ILTS_PIK, IMAU, JPL, LSCE, NCAR, UCI_JPL, and VUB (Goelzer et al., 2020; Seroussi et al., 2020). Ice-sheet modeling groups considered here work under the framework of the Ice Sheet Model Intercomparison Project for CMIP6 (ISMIP6). These projections include the historical contributions from deglacial mass change and Little Ice Age mass change, as well as the projected contributions from thermal expansion, ocean dynamics, global glacier change, and land water storage.

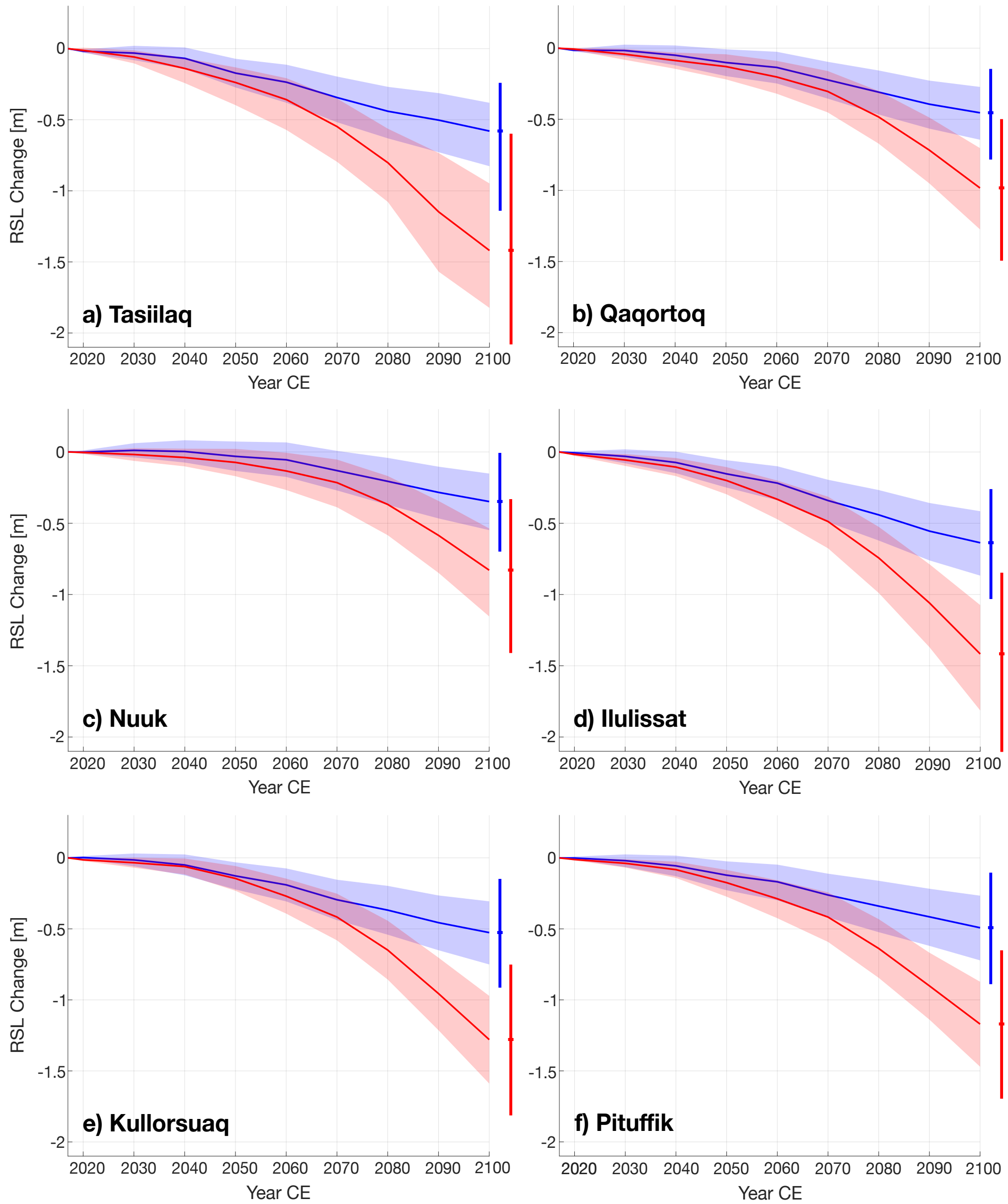

Supplementary Figure 5: **Projections of relative sea level (RSL) to 2100 CE for six settlements along Greenland's coast**. Projections are shown for RCP 2.6 (blue) and RCP 8.5 (red) in : Tasiilaq a), Qaqortoq b), Nuuk c), Ilulissat d), Kullorsuaq e), Pituffik f). Locations of these settlements are shown by the white stars in Fig. 5c. The solid line represents the ensemble median and the shaded region is the likely range (17^{th}-83^{rd} percentile). The bars on the right represent the 5th-95th percentile range of projected RSL at 2100 CE.

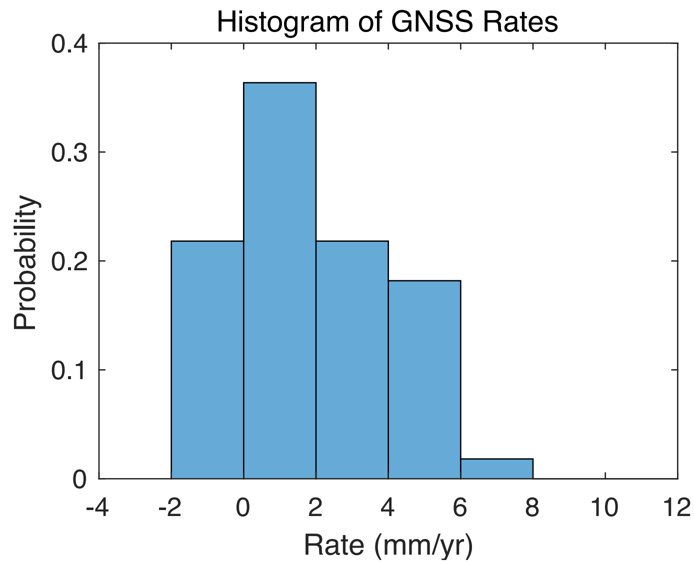

Supplementary Figure 6: **Histogram of GNSS VLM rates.** Rates from $N = 55$ GNSS locations have been corrected for elastic and deglacial contributions (LIA' VLM).

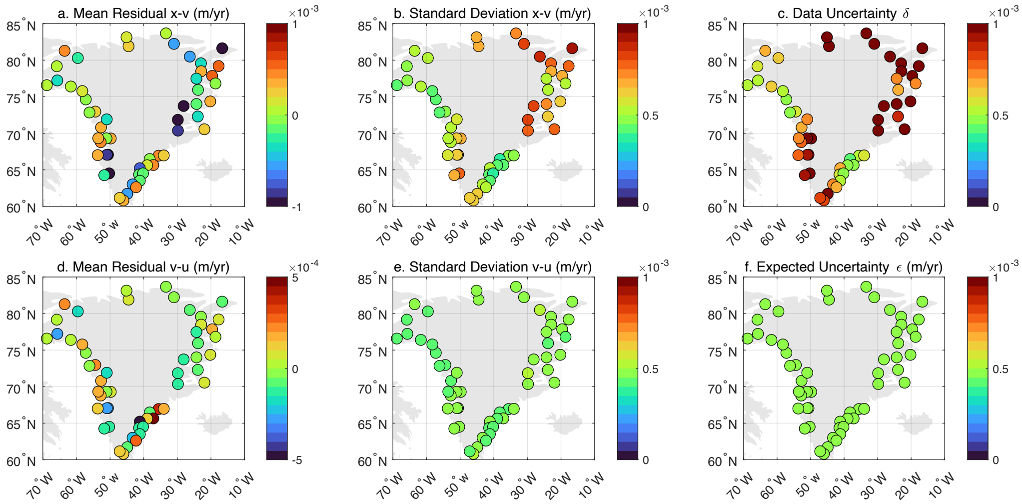

Supplementary Figure 7: **Residual analysis for the Bayesian model**. Means a) and standard deviations b) of residual differences $x - v$ between LIA' VLM observations x and full Bayesian rate solutions v at the $N = 55$ GNSS locations (m/yr; Equation 4). c) Standard errors on LIA' VLM data x at GNSS locations (m/yr). Means d) and standard deviations e) of residuals $v - u$ between full Bayesian rate solutions v and large-scale rate solutions u at GNSS locations (m/yr). f) Expected uncertainty ϵ on $v - u$ residuals (m/yr); values are computed as the mean of the square root of posterior solutions for the parameter ϵ^2.

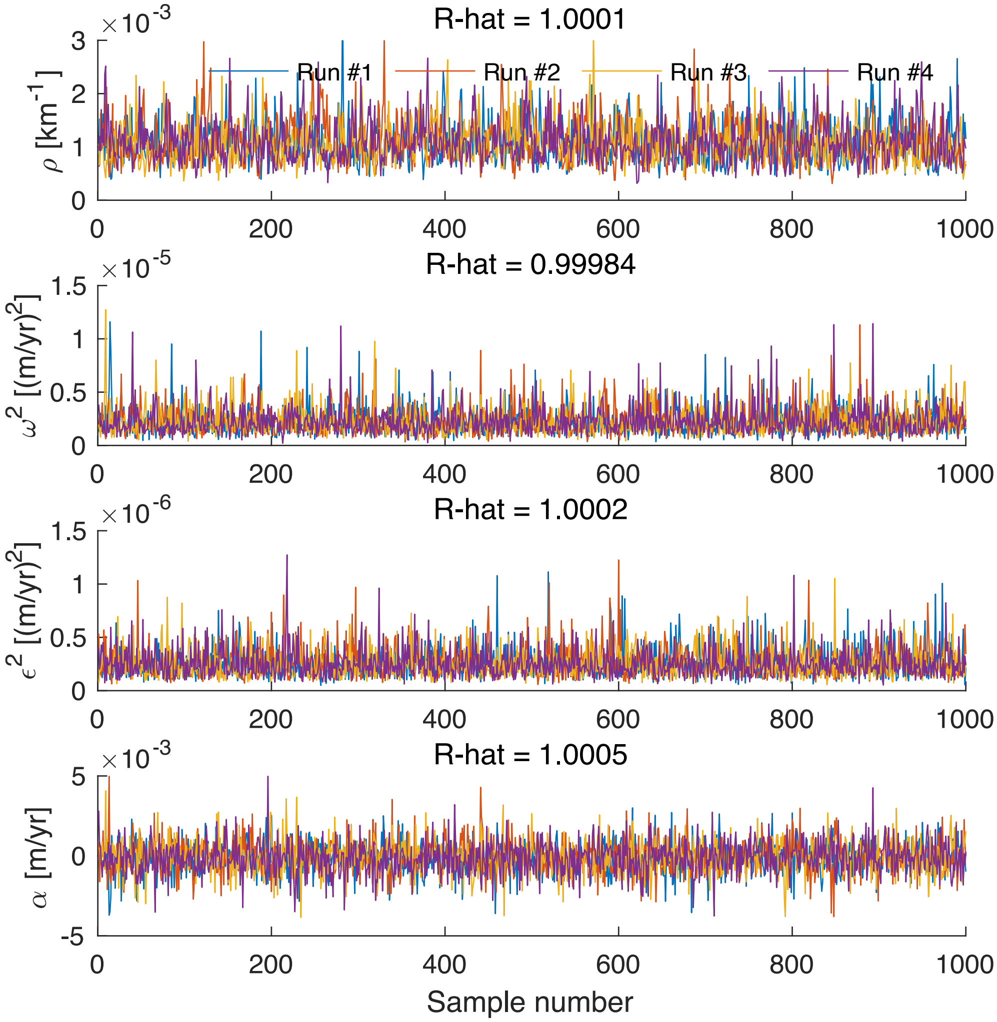

Supplementary Figure 8: **Convergence analysis for the Bayesian model.** Trace plots of posterior scalar parameter solutions. Respective parameters are identified along the vertical axes. The plots were generated by performing four separate runs of the Bayesian model with randomized initial conditions to quantify convergence. For each plot, the R-hat (Gelman-Rubin) statistic for that parameter is given. R-hat values are universally ~1, which indicates the solutions have converged.

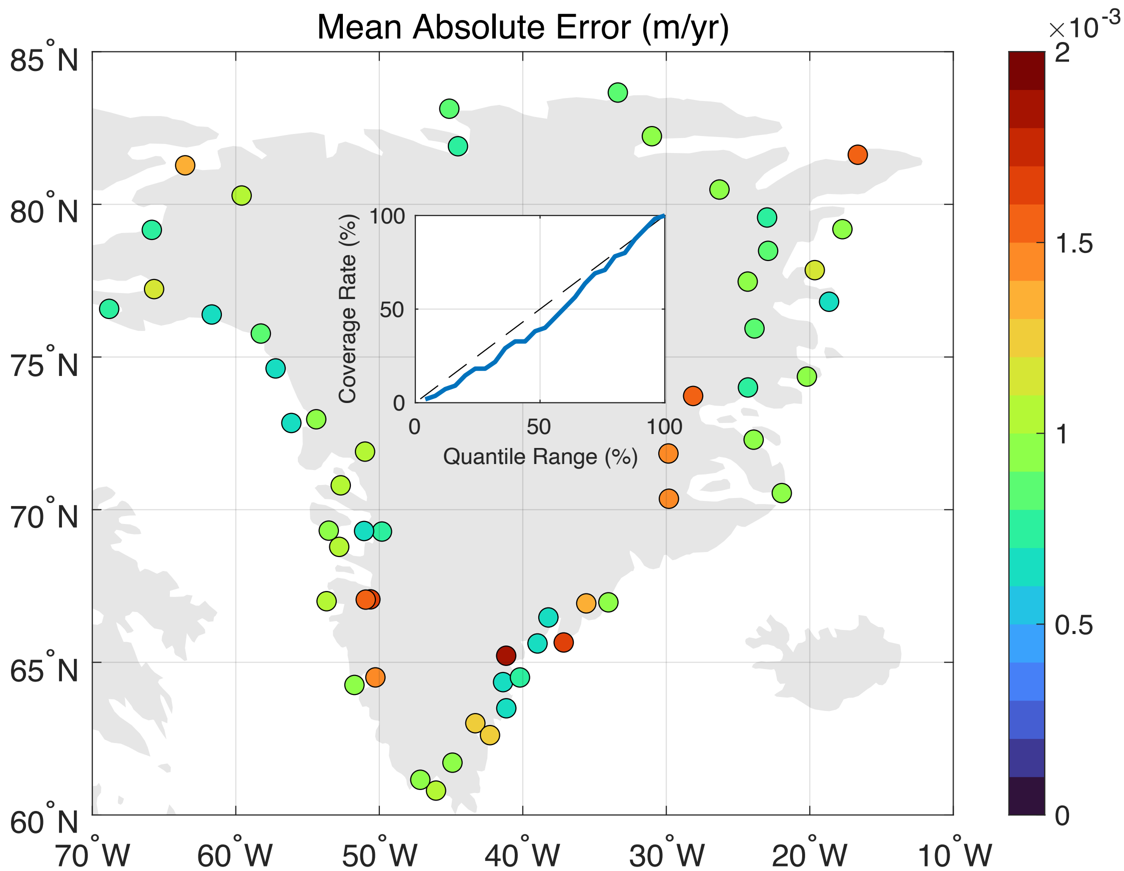

Supplementary Figure 9: **Results from leave-one-out cross-validation experiments**. Colored dots show mean absolute error between model prediction and withheld observation at each of the GNSS location from the corresponding leave-one-out cross-validation experiment (m/yr). Inset shows coverage rates. The blue solid line delineates the percentage coverage rate (i.e., percent of true withheld values captured by the model's posterior credible intervals) as a function of quantile range, while the black dashed line shows the target 1-to-1 line.

References

1. Afonso, J. C., Salajegheh, F., Szwillus, W., Ebbing, J. & Gaina, C. A global reference model of the lithosphere and upper mantle from joint inversion and analysis of multiple data sets. *Geophysical Journal International* **217**, 1602–1628 (2019).
2. Antwerpen, R. *et al.* Holocene southwest Greenland ice sheet behavior constrained by sea-level modeling. *Quaternary Science Reviews* **328**, 108553 (2024).
3. Austermann, J., Hoggard, M. J., Latychev, K., Richards, F. D. & Mitrovica, J. X. The effect of lateral variations in Earth structure on Last Interglacial sea level. *Geophysical Journal International* **227**, 1938–1960 (2021).
4. Goelzer, H. *et al*. The future sea-level contribution of the Greenland ice sheet: a multi-model ensemble study of ISMIP6. *The Cryosphere* **14**, 3071–3096 (2020).
5. Hill, E. M., Davis, J. L., Tamisiea, M. E. & Lidberg, M. Combination of geodetic observations and models for glacial isostatic adjustment fields in Fennoscandia. *Journal of Geophysical Research: Solid Earth* **115** (2010).
6. Lidberg, M., Johansson, J. M., Scherneck, H. G. & Davis, J. L. An improved and extended GPS-derived 3D velocity field of the glacial isostatic adjustment (GIA) in Fennoscandia. *Journal of Geodesy* **81**, 213–230 (2007).
7. Pan, L. *et al*. The influence of lateral Earth structure on inferences of global ice volume during the Last Glacial Maximum. *Quaternary Science Reviews* **290**, 107644 (2022).
8. Peltier, W. R. Global glacial isostasy and the surface of the ice-age Earth: the ICE-5G (VM2) model and GRACE. *Annu. Rev. Earth Planet. Sci. 32***(1)**, 111-149 (2004).

9. Peltier, W. R., & Drummond, R. Rheological stratification of the lithosphere: A direct inference based upon the geodetically observed pattern of the glacial isostatic adjustment of the North American continent. *Geophysical Research Letters* ***35*****(16)**, (2008)
10. Seroussi, H. *et al*. ISMIP6 Antarctica: a multi-model ensemble of the Antarctic ice sheet evolution over the 21st century. *The Cryosphere Discussions* **14**, 1–54 (2020).
11. Yousefi, M., Milne, G. A., & Latychev, K. Glacial isostatic adjustment of the Pacific Coast of North America: the influence of lateral Earth structure. *Geophysical Journal International*, **226(1)**, 91-113 (2021).